CHAPTER 5:

EROSION BEHAVIOR OF DUAL PHASE STEELS AT DIFFERENT IMPACT ANGLES AND VELOCITIES

CHAPTER 5

EROSION BEHAVIOR OF DP STEELS AT DIFFERENT IMPACT ANGLES AND VELOCITIES

This chapter presents the results on the erosive wear of medium carbon normalized (N), dual phase (DP) and fully martensitic (FMS) steels at different velocities (30 m/s, 60 m/s, 90 m/s and 120 m/s) and impingement angles (15°, 45°, 75°, and 90°) with Al_2O_3 as an erodent. The results on microstructural and sub-surface analysis conducted to understand the mechanisms of material removal are also included in the chapter. The chapter also contains a comprehensive discussion on the observed erosive behavior of different steels correlating it with the microstructural features seen on the surface and sub-surface of the eroded steels apart from their mechanical properties. A mechanism of material removal has also been proposed for N, DP and fully martensitic steel having different microstructures.

5.1 RESULTS

5.1.1 Erosive wear at different impact velocity and impingement angles

The optical, scanning electron and transmission electron micrographs for normalized (N), dual Phase (DP) and fully martensitic steels developed through heat treatment of medium carbon steel have already been presented in chapter 3**.** The hardness of N, DP2, DP3, DP3.5, DP4, and FMS steels, respectively, are 210 HV, 285 HV, 387 HV, 391 HV, 423 HV and 525 HV. N steel has shown the lowest hardness and FMs has the highest. The hardness of DP steels is found to lie between N steel and FMS. One may also observe

that the hardness of DP steels increases with increasing amount of martensite as one move from DP2 (39% martensite) to DP4 steel (79 % martensite). The ultimate tensile strength (UTS) and Yield strength (YS) have also been found to increase with increasing amount of martensite in DP steels whereas the % EL has been observed to decrease. N steel has shown the lowest UTS & YS and the highest % EL whereas, FMS has shown the highest UTS &YS and the lowest % EL among all the steels used in the current study as stated in Chapter 4 also.

Figure 5.1 shows the variation of erosion rate with time for all the steels at 15° and 90° impact angles and 30 m/s and 120 m/s impact velocities. The steady state has been observed to be attained after 20 to 30 minutes (approx.) for all the steels as seen from Figs. 5.1 (a through d). One may observe that different steels took different times to reach a steady state indicating that attainment of steady state depends on the microstructure, impact velocity and angle of impact. In the current investigation, steady state erosion rate has been used to study erosive of steels.

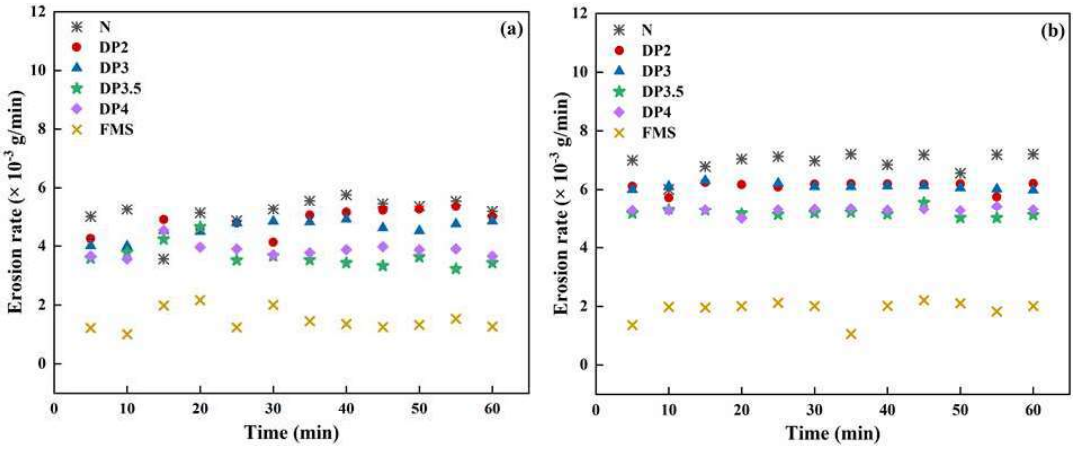

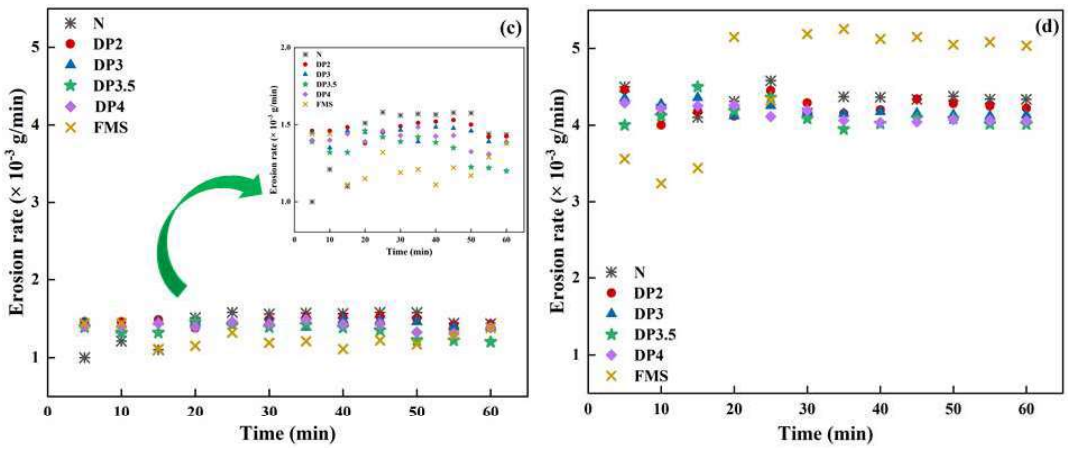

Figure 5.1 Variation of erosion rate with time for (a) 15° and 30 m/s, (b) 15° and 120 m/s, (c) 90° and 30 m/s, and (d) 90° and 120 m/s

The variation of steady state erosion rate with initial hardness for various impact velocities of (30 m/s, 60 m/s, 90 m/s and 120 m/s) at different angles of impingement is illustrated in Figs. 5.2 (a through d): Consequently, it is evident that at a given angle of impact, the steady state erosion rate of all the materials, including N steel, DP steels and FMS, reduces with increasing hardness. The maximum weight loss of 1.42×10^{-3} g is observed for N steel (210HV3) at particle velocity of 120 m/s and 15° impact angle which is 8 %, 16 % and 29 % higher corresponding to that at 30 m/s, 60 m/s and 90 m/s, respectively. FMS (590 HV3) has shown the minimum weight loss of 2.84×10^{-4} g (FMS) at 30 m/s impact velocity and 15° impact angle which is 9 %, 30 % and 38 % lower than that observed at 60 m/s, 90 m/s and 120 m/s as seen from Fig. 5.2. DP steels have shown the erosion rates lying between this of N steel and FMS. However, as one progresses from DP2 to DP4 steel among DP steels, the erosion rate decreases with increasing hardness, as seen in Fig. 5.2 (a). A similar trend of variation is also observed from a 45° angle of impact as illustrated in Fig. 5.2 (b). However, the rate of decrease of

erosion rate is relatively less at an impact angle of 45° than at 15° as evident from a comparison of Figs. 5.2 (a) and (b).

It was evident that the erosion rate of N steel and DP steels are almost same at 75° angle of impingement and at relatively lower velocities of 30 m/s and 60 m/s indicating that there is no effect of hardness as seen from Fig. 5.2 (c). However, N steel has a marginally higher erosion rate than DP steels at relatively higher velocities of 90 m/s and 120 m/s. The effect of hardness on erosion rate could be seen beyond a hardness of 423HV3 corresponding to DP4 steel only as seen from Fig. 5.2 (c) which indicates a decrease in erosion rate till FMS. One may also observe that the decrease in erosion rate beyond DP4 is higher at relatively higher velocities of 90 m/s and 120 m/s as compared to 30 m/s and 60 m/s. All the materials have shown almost the same erosion rates for all the velocities at an impact angle of 90°, as shown in Fig. 5.2 (d), reflecting no effect of hardness on material loss except for FMS at 120 m/s which has shown the highest erosion rate.

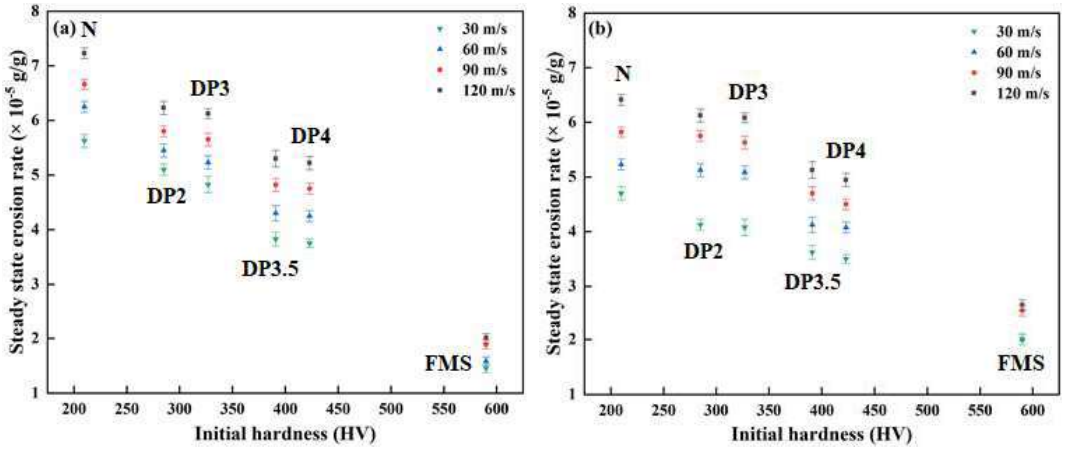

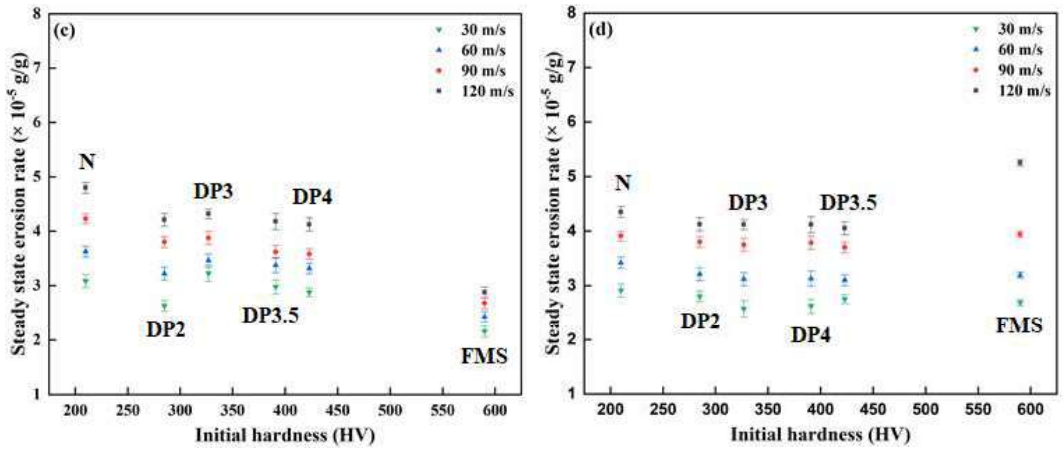

Figure 5.2 Variation of steady state erosion rate with initial hardness for impact velocity of 30 m/s, 60 m/s, 90 m/s 120 m/s, and at an impact angles of (a) 15°, (b) 45°, (c) 75°, and (d) 90°, respectively

Figures 5.3 ((a) through (d)) illustrate the variation of steady state erosion rate with impact velocity for the N steel, DP steels and FMS at different angles of impingement. Where the steady state erosion rate of all materials increases with increasing velocity of impact at all angle of impact. However, N steel has shown the maximum erosion rate whereas FMS has shown the minimum erosion at all the velocities and angles of impingement except at 90° and 120 m/s where FMS has shown the highest rate of wear, see Fig. 5.3 (d). The erosion rates of DP steels are found to lie in-between those shown by N steel and FMS. Among DP steels, both DP2 & DP3 steels have shown the same erosion rate at impact angles of 15° and 45° as seen from Fig. 5.3 (a). The erosion rates observed for DP3.5 & DP4 steels at 15° and 45° are almost the same, displayed in Fig. 5.3 (b), however, the erosion rates shown by DP3.5 and DP4 steels are significantly lower than those of DP2 & DP3 steels as evident from a comparison of Figs. 5.3 ((a) and (b)). At relatively higher impact angles i.e., 75° & 90° the difference between erosion

rates of DP steels is marginal at relatively lower velocities of 30 m/s and 60 m/s, however, the erosion rates appear to be similar at velocities of 90 m/s and 120 m/s. It is also evident that the gap in erosion rates between N steel, DP steels and FMS narrows as one moves from 15° to 90° impact angles and the erosion rates of all materials fall in the same band, as shown in Figs. 5.3 ((a) through (d)).

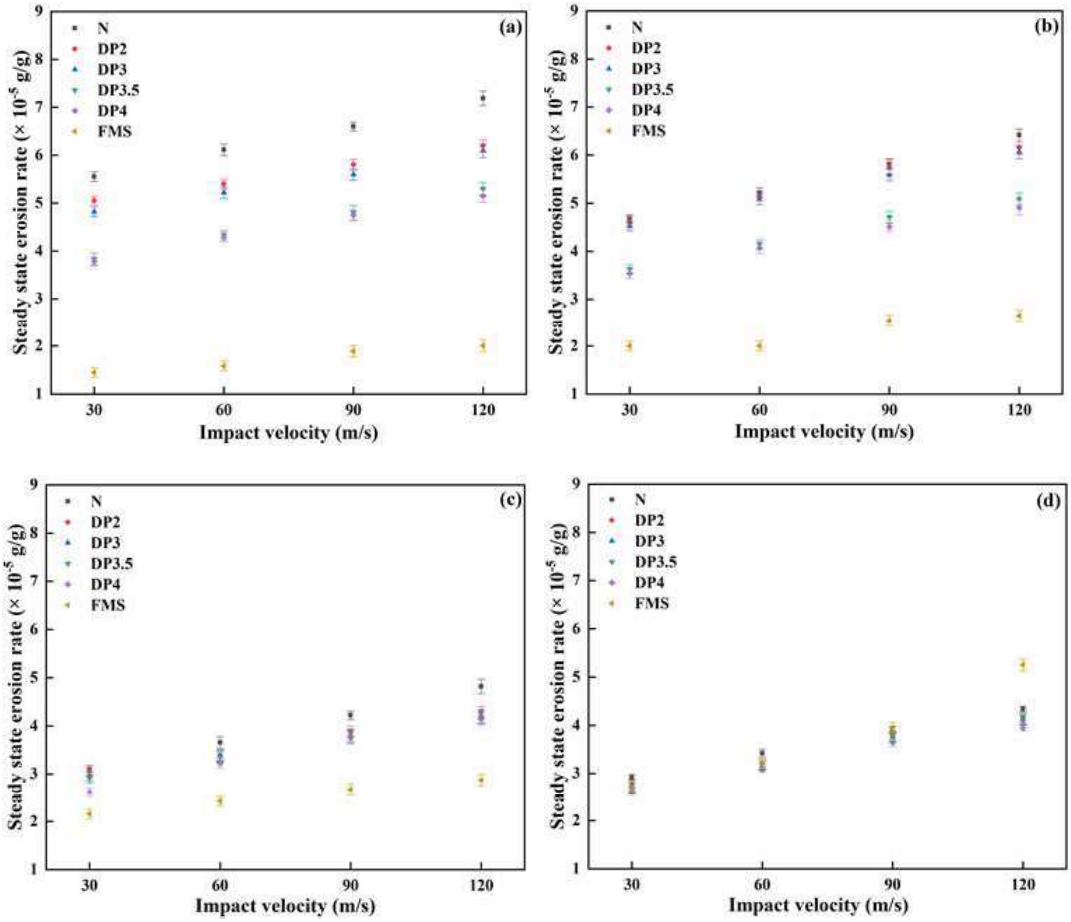

Figure 5.3 Variation of steady state erosion rate with impact velocity for the N steel, DP steels and FMS at impact angles of (a) 15°, (b) 45°, (c) 75°, and (d) 90°, respectively

Figures 5.4 ((a) through (d)) illustrate the variation of steady state erosion rate with impingement angle for N steel, DP steels and FMS at various impact velocities. It could be seen that at particular angle of impact, the steady state erosion rate of N steel and DP

steels decrease with increasing impingement angles and the trend of variation is same for both. However, for FMS the erosion rate increases as the impingement angle is increased from 15° to 90° as evident from Figs. 5.4 ((a) through (d)). N steel has the highest erosion rate and FMS has the lowest except at 90° and 120 m/s, see Fig. 5.4 (d) which has been indicated earlier also by Fig. 5.4 (d). One may also observe that for relatively lower angles of impact i.e., 15° and 45° the gap between erosion rates of N and DP2 steels increases with increasing velocity of impact from 30 m/s to 120 m/s. The same is also true for erosion rates of DP4 steel and FMS.

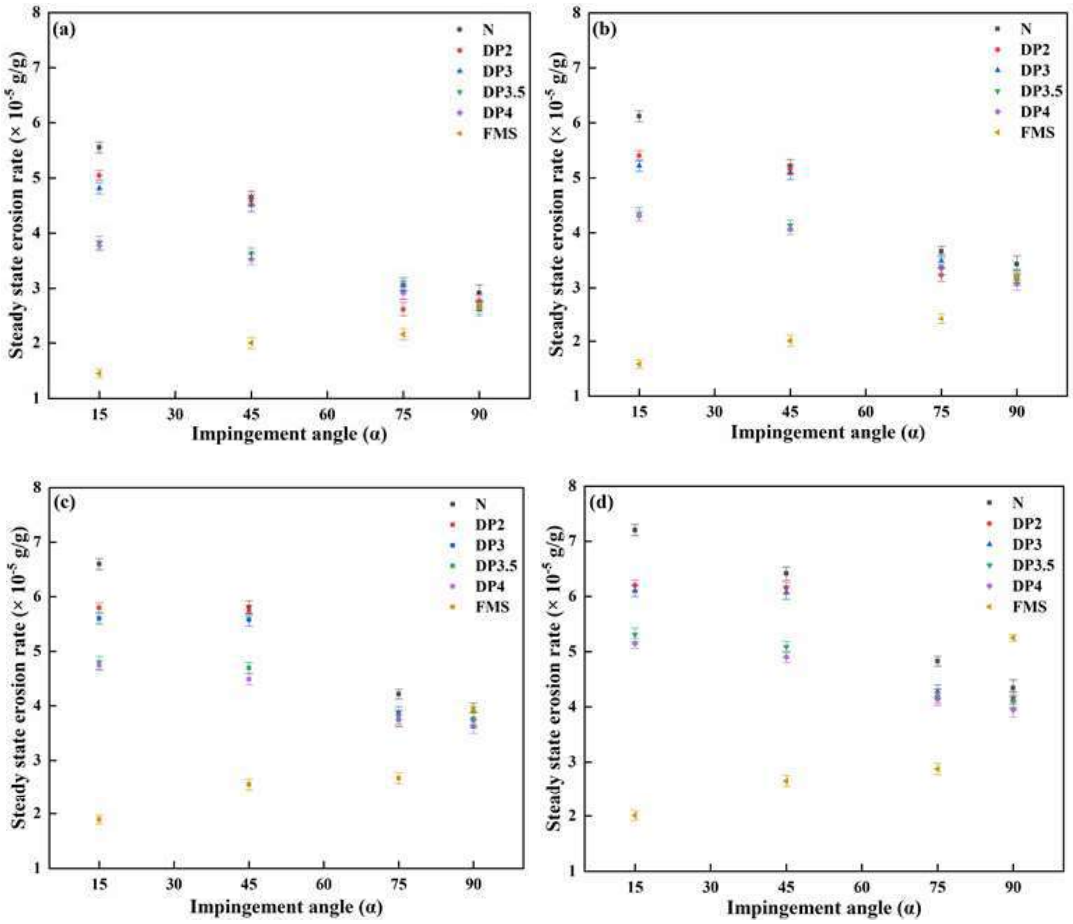

Figure 5.4 Variation of steady state erosion rate with impingement angle for the N steel, DP steels and FMS at impact velocities of (a) 30 m/s, (b) 60 m/s, (c) 90 m/s, and (d) 120 m/s, respectively

5.1.2 Examination of eroded surfaces

In order to examine eroded surfaces, four different operating conditions were taken into consideration which is listed in Table 5.1. SEM micrographs of N steel, DP steels and FMS at 30 m/s and 15° impact angle are depicted in Figs. 5.5 ((a) through (f)). N steel exhibits deep micro ploughing, formation of lateral lips and ridge formation as seen from Fig. 5.5 (a), whereas DP2 steel reveals the presence of multiple shallow micro cutting as well as ridge formation and deep micro ploughing marks as seen from Fig 5.5 (b). The eroded surface of DP3 steel has deep micro ploughing marks, while the surface of DP3.5 steel has shallow ploughing marks and craters, see Figs. 5.5 ((c) and (d)). The eroded surfaces of DP4 steel and FMS exhibit a few micro ploughing marks, as depicted in Figs. 5.5 ((e) through (f)).

Table 5.1 Different conditions used for analysis of eroded surfaces

Conditions		Impact angle	Impact Velocity
i.	Low angle-Low velocity	15°	30 m/s
ii.	Low angle-High velocity	15°	120 m/s
iii.	High angle-Low velocity	90°	30 m/s
iv.	High angle-High velocity	90°	120 m/s

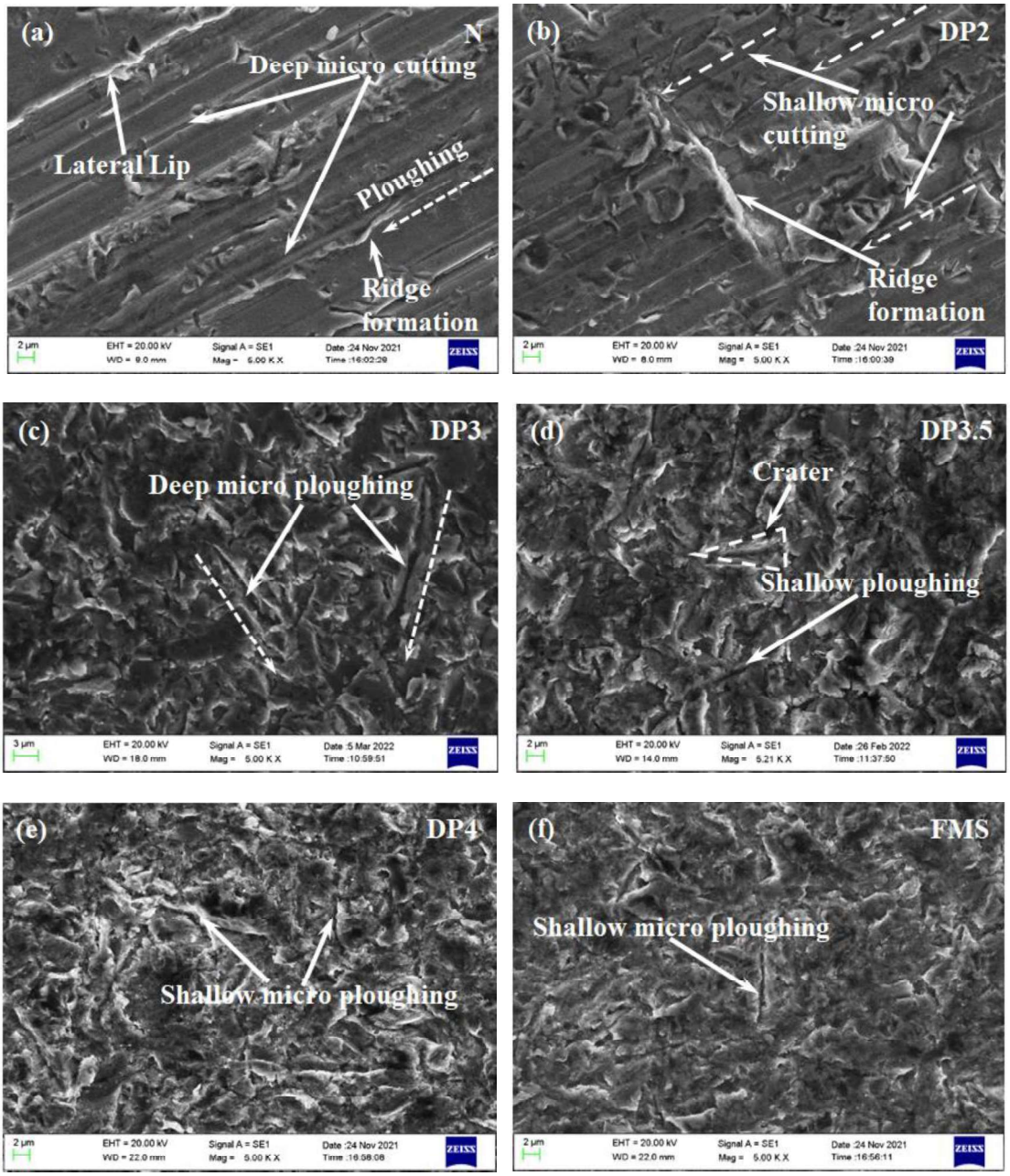

Figure 5.5 SEM micrographs of eroded surface of (a) N steel, (b) DP2 steel, (c) DP3 steel, (d) DP3.5 steel, (e) DP4 steel, and (f) FMS at 30 m/s and 15° angle of impact

In Fig. 5.6 (a), a SEM micrograph of the surface of N steel that has been eroded at 30 m/s and a 90° angle of impact reveals the existence of plastic deformation and flattened ridges, whereas in Fig. 5.6 (b), a SEM micrograph of the surface of DP2 steel that has

also been eroded exhibits the occurrence of plastic deformation exclusively. The micrograph of DP3 steel shows the features of low angle cutting and flattened ridges see Fig. 5.6 (c) and that of DP3.5 steel exhibits crater and chip formation apart from low angle cutting as seen from Fig. 5.6 (d). The DP4 steel and FMS reveal the presence of shallow craters and chips along with low angle cutting as shown in Figs. 5.6 ((e) - (f)).

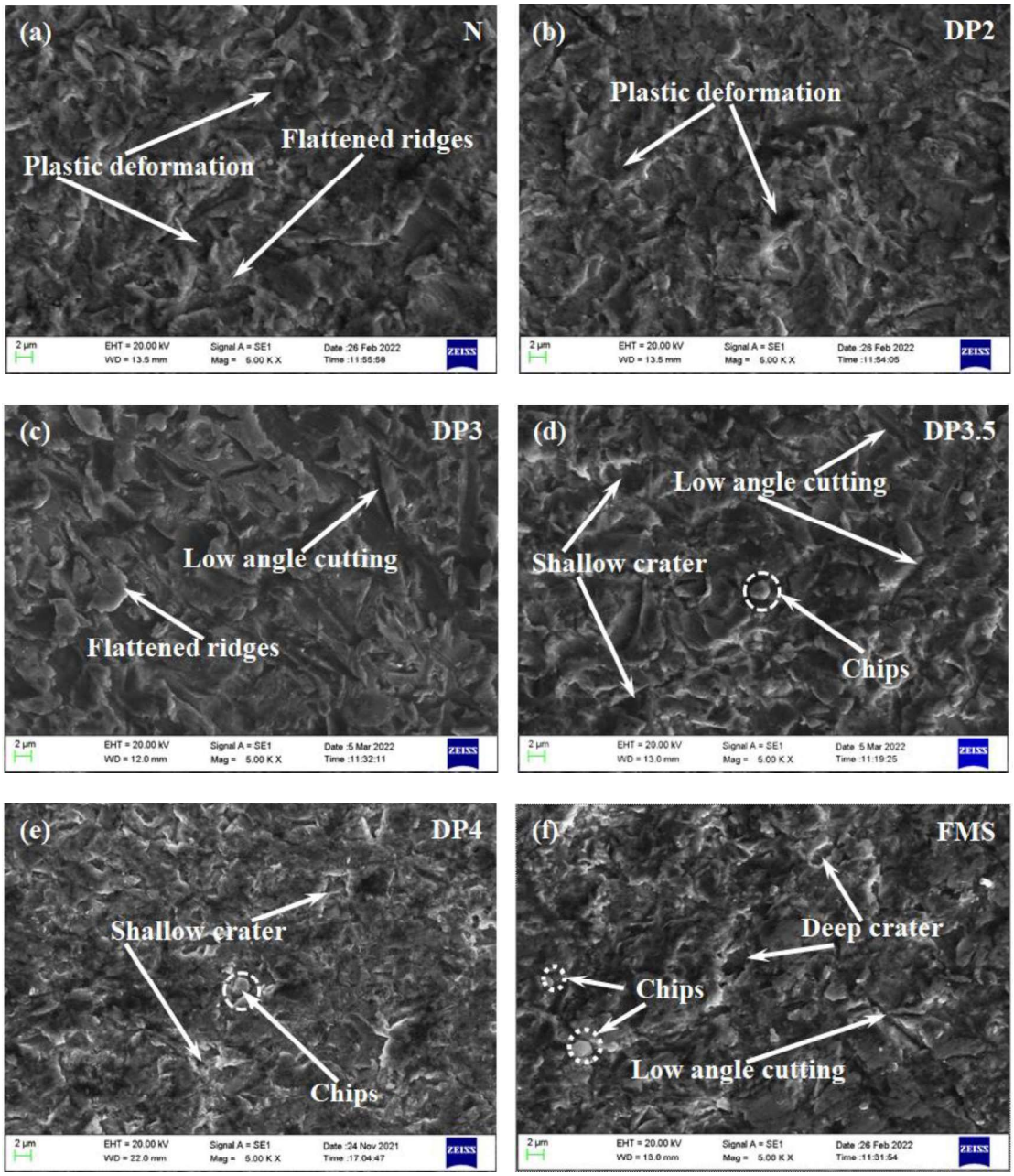

Figure 5.6 SEM micrographs of eroded surface of (a) N steel, (b) DP2 steel, (c) DP3 steel, (d) DP3.5 steel, (e) DP4 steel, and (f) FMS at 30 m/s and 90° angle of impact

A SEM micrograph of the eroded surface of N steel is shown in Fig. 5.7 (a) and it reveals that, aside from the formation of a frontal lip at 120 m/s and a 15° angle of impact, deep micro ploughing and plastic deformation also occurred. The micrograph of DP2 steel reveals the presence of micro cutting and micro ploughing at several places, formation of crater and chips along with embedded Al_2O_3 particles and flattened ridges as seen from Fig. 5.7 (b). The DP3 steel shows the presence of the Al_2O_3 particle embedded into the surface near the tip of the ploughing path and signs of plastic deformation see Fig. 5.7 (c). Whereas that of DP3.5 steel reveals deep micro ploughing only as seen from Fig. 5.7 (d). As shown in Figs. 5.7 ((e) and f)), there have been shallow micro-ploughing marks on the eroded surfaces of DP4 steel and FMS.

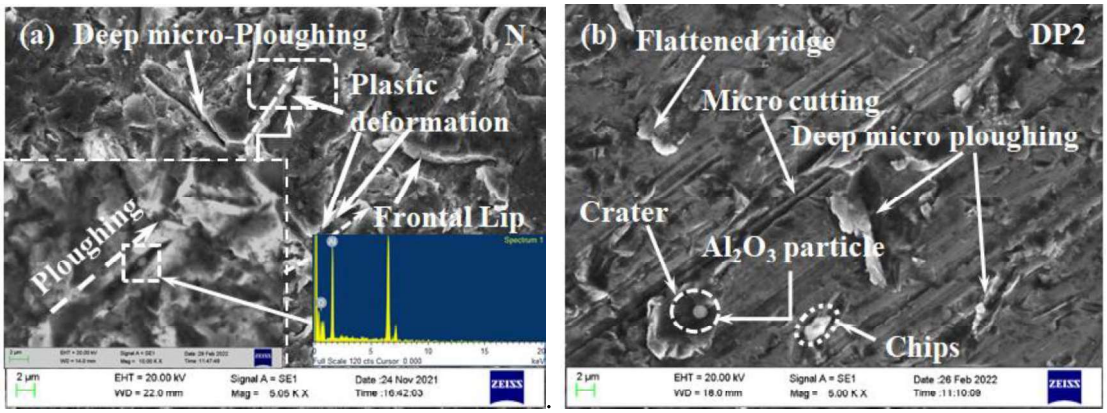

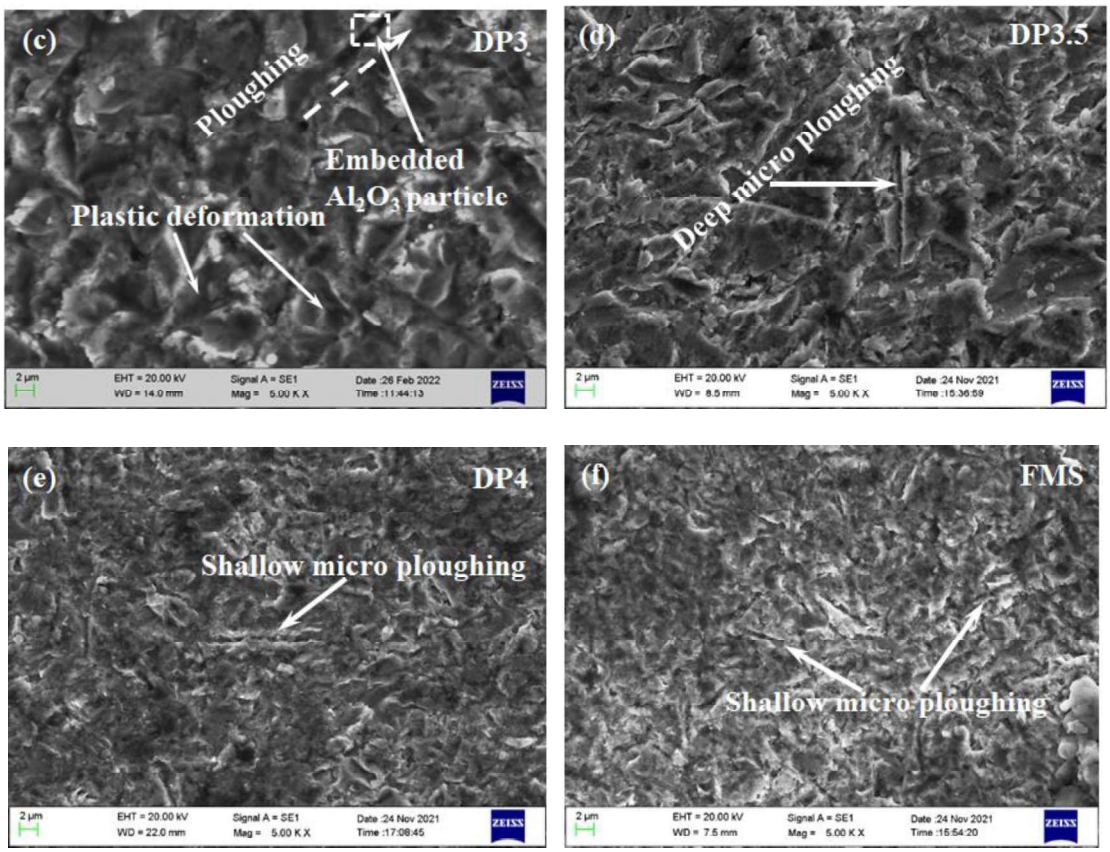

Figure 5.7 SEM micrographs of eroded surface of (a) N steel, (b) DP2 steel, (c) DP3 steel, (d) DP3.5 steel, (e) DP4 steel, and (f) FMS at 120 m/s and 15° angle of impact

Figs. 5.8 ((a) - (f)) depicts SEM micrographs of the eroded surface of N steel, DP steels and FMS at 120 m/s and 90° impact angle. The embedment of erodent particles, low angle cutting and ridge formation could be observed in N steel as seen in Fig. 5.8 (a) whereas embedded particles and metal chips could be noticed in DP2 steel, displayed in Fig. 5.8 (b). Shallow craters and embedded particles could be observed on the eroded surface of DP3 steel in Fig. 5.8 (c), whereas, as seen in Fig. 5.8 (d), the eroded surface of DP3.5 steel exhibits deep craters, low angle cutting and embedded particles. The eroded surface of DP4 steel exhibits the presence of deep and shallow craters whereas deep

craters as well as extruded lip are found to be present on the surface of FMS as shown in Figs. 5.8 ((e) and (f)), respectively.

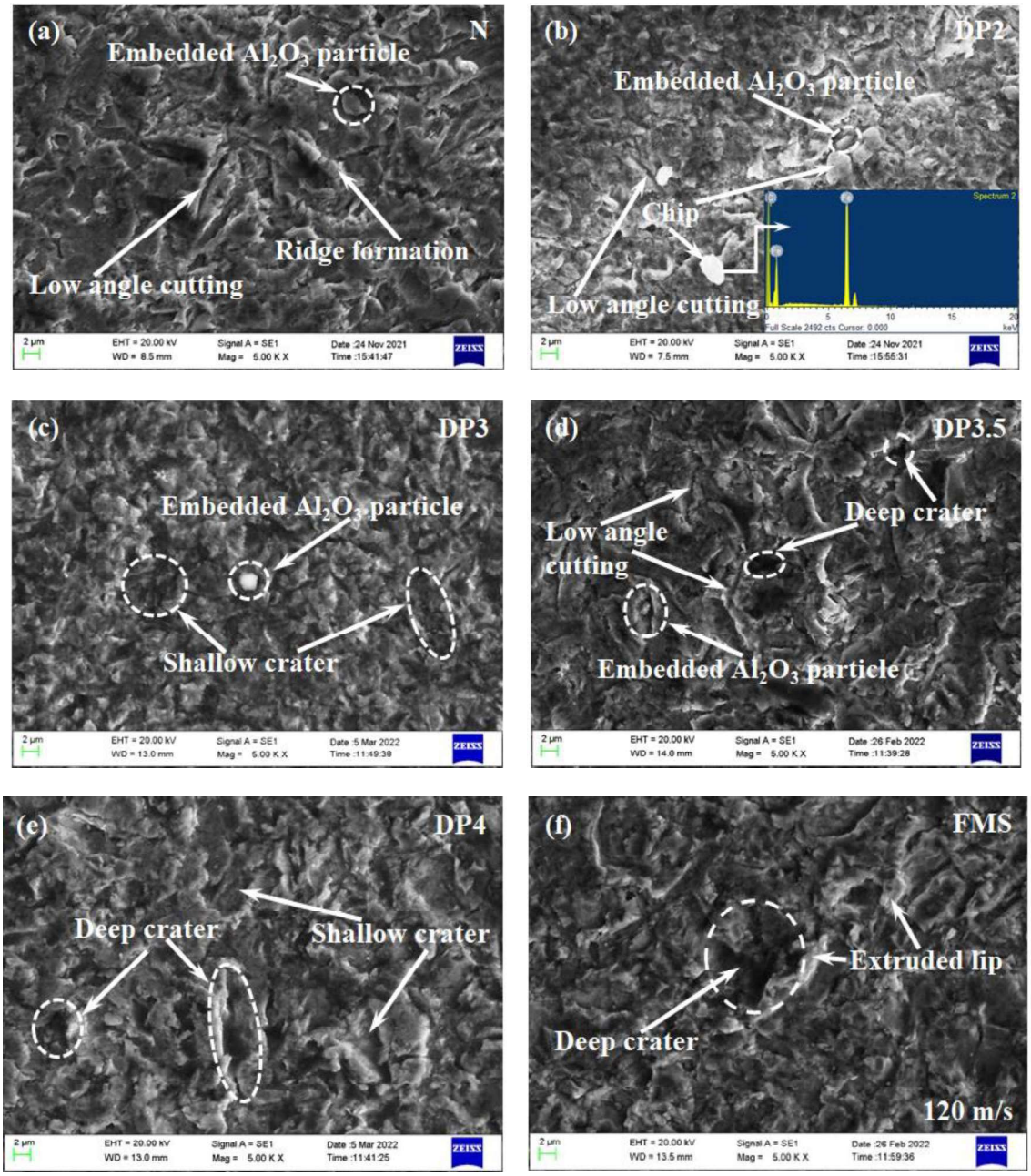

Figure 5.8 SEM micrographs of eroded surface of (a) N steel, (b) DP2 steel, (c) DP3 steel, (d) DP3.5 steel, (e) DP4 steel, and (f) FMS at 120 m/s and 90° angle of impact

In order to analyze the extent of damage due to impact of erodent, the cross-sections of eroded specimens of N steel, DP3.5 steel and FMS after the erosion tests at 15° impingement angle and 120 m/s impact velocity i.e., low angle-high velocity, 90° and 30 m/s i.e., high angle-low velocity and 90° and 120 m/s i.e., high angle-high velocity have been examined under SEM and the images are presented in Figs. 5.9, 5.10, and 5.11. One may observe that plastically deformed region extends up to the depths of 78.5 μm, 35.6 μm and 18.78 μm for low angle-high velocity for N steel, DP3.5 steel and FMS, respectively, as depicted in Figs. 5.9 ((a) - (c)), whereas the same extends up to the depths of 46.56, 18.98 and 4.87 μm for high angle-low velocity condition as seen from Figs. 5.10 ((a) - (c)). However, at high angle-high velocity condition the plastic deformation extends up to the depths of 126.23 μm, 101.36 μm and 45.22 μm as seen from Figs. 5.11 ((a) – (c)). This reflects the severity of deformation in high angle-high velocity condition in comparison to low angle/high angle-low velocity. Also, the accumulation of deformed material could be observed beneath the eroded surface of N steel as shown in the inset of Fig. 5.9 (a), whereas the DP3.5 steel reveals the presence of ridges as depicted in the inset of Fig. 5.9 (b). However, the presence of micro crack could be seen below the eroded surface of FMS as illustrated in the inset of Fig. 5.9 (c). The fractured cementite plates could be observed on the deformed zone of N steel beneath the eroded surface due to the plastic deformation as observed in the inset of Fig. 5.10 (a). The bright & hardened deformed layer could be seen on DP3.5 steel, whereas hardly any deformed layer could be observed in FMS due to its high hardness as shown in Figs. 5.10 ((b) and (c)). Some micro cutting features and chips are visible on the subsurface of N Steel whereas chips and subsurface cracks at 30.93 μm from the eroded

surface could be seen for DP3.5 as shown in Fig. 5.11 ((a) and (b)). However, micro cracks may be observed at the subsurface of the eroded FMS specimen as seen in the inset of Fig. 5.11 (c).

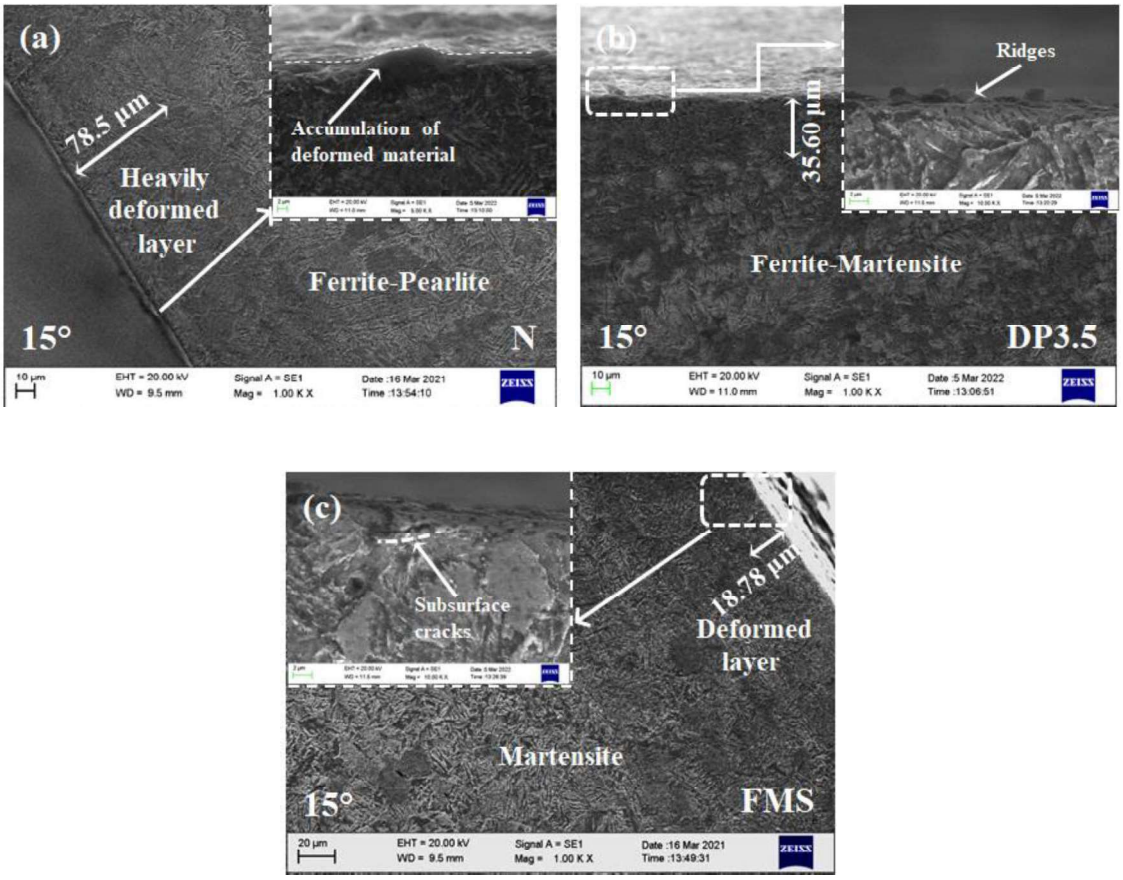

Figure 5.9 SEM micrographs of cross section of (a) N steel, (b) DP3.5 steel, and (c) FMS, respectively, at 120 m/s and 15° angle of impact

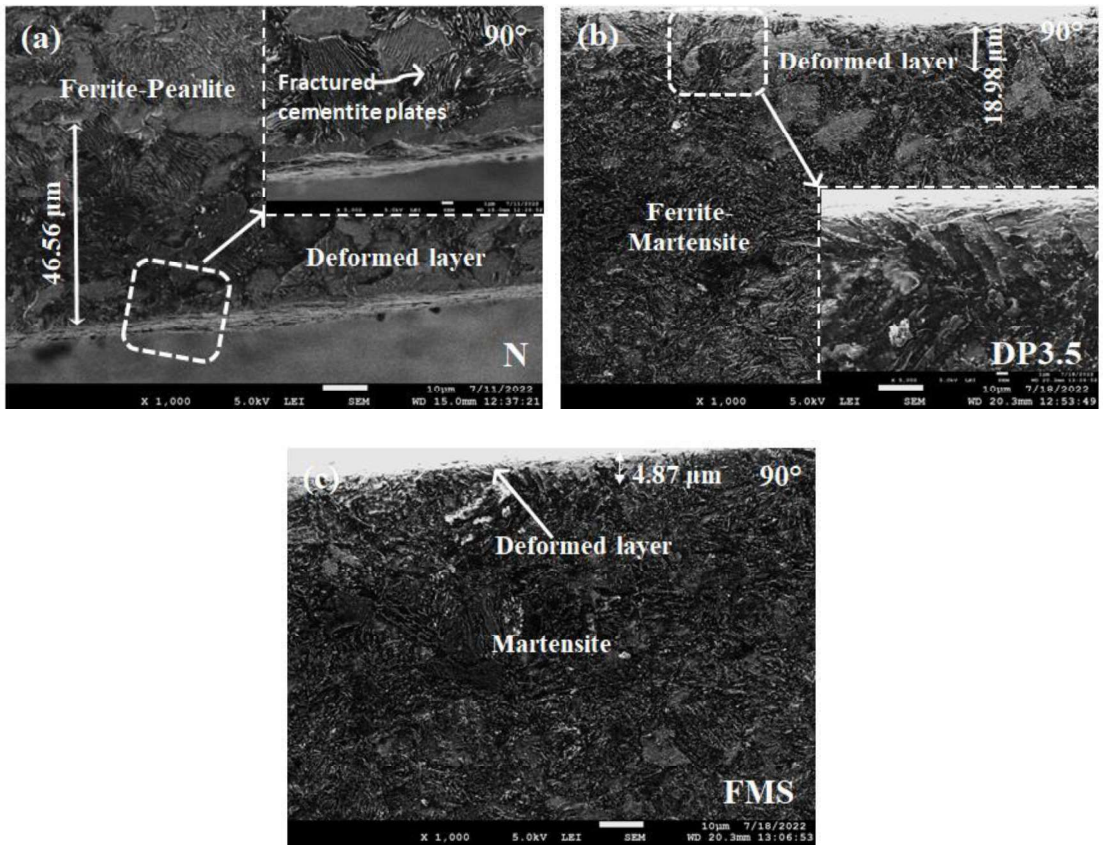

Figure 5.10 SEM micrographs of cross section of (a) N steel, (b) DP3.5 steel, and (c) FMS respectively, at 30 m/s and 90° angle of impact

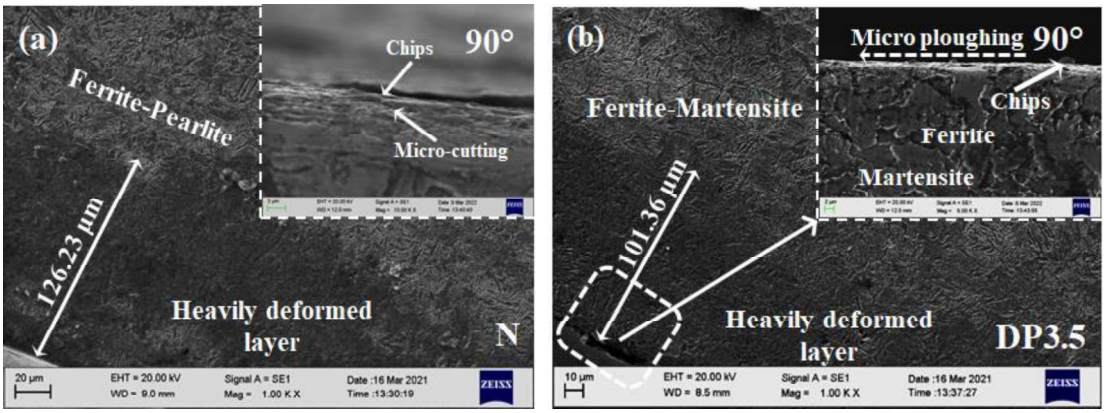

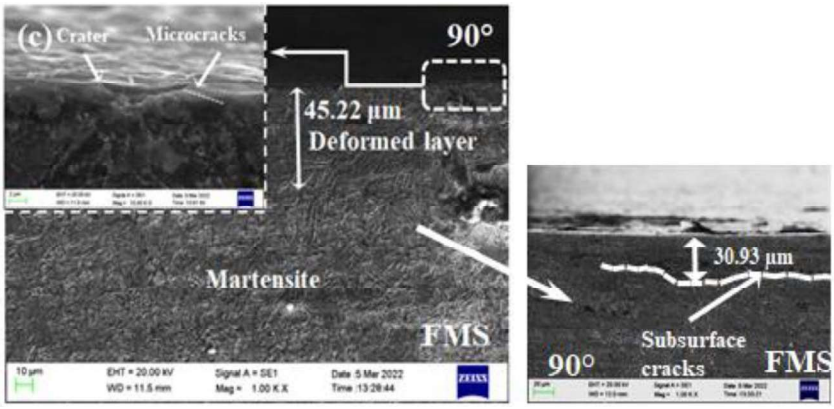

Figure 5.11 SEM micrographs of cross section of (a) N steel, (b) DP3.5 steel, and (c) FMS respectively, at 120 m/s and 90° impact angle

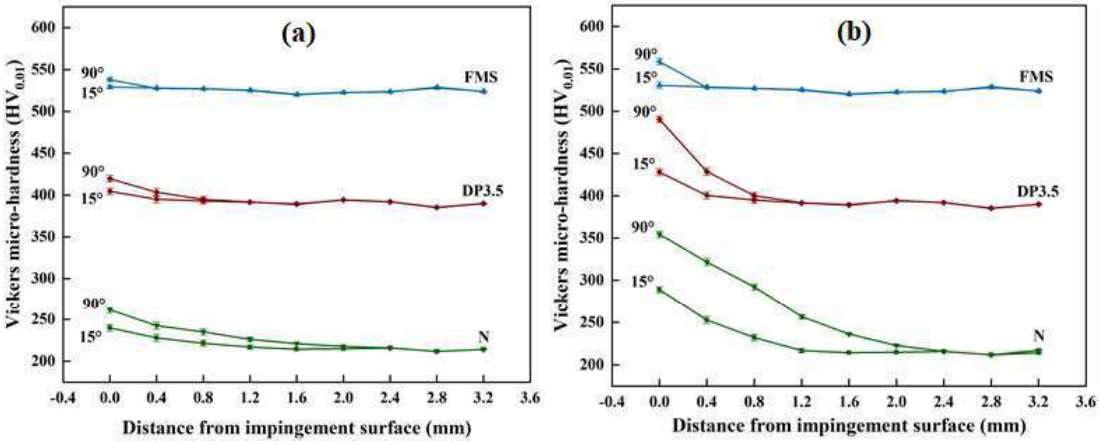

Figure 5.12 Micro-hardness profile of the eroded specimens of the N steel, DP3.5 steel and FMS at 15 and 90° angle of impact at (a) 30 m/s and (b) 120 m/s impact velocity

5.2 DISCUSSION

The hardness of DP steels increases progressively from DP2 to DP4 steel due to an increase in the hard martensite phase. FMS has the highest level of hardness among the materials investigated in this study because it contains the highest amount of martensite. The increased amount of martensite, a strong and load-bearing phase, is also responsible for the increase in tensile and yield strength and the decrease in % EL and toughness.

The observed behavior is in consonance with the results reported earlier [9,94,95]. Hardness and toughness are the main properties that influence the erosive behavior of a material, and these are dependent on the microstructure of the material being impacted. Hence, the erosive wear of these steels is expected to be governed by their microstructures. A decrease in steady state erosion rate with an increase in hardness for all steels as illustrated in Figs. 5.2 ((a) - (d)) may be explained on the basis of the features seen from the SEM images of the eroded specimens.

An increase in steady-state erosion rate with increasing velocity at normal incident angle for N steel, DP steels and FMS as seen in Figs. 5.3 ((a) - (d)) may be attributed to the erosion caused by alumina particles depending on the impact velocity and angle. The repetitive impact of erodent on the surface of steel results in work hardening and subsequent fragile fracture of material, which may be inferred from the occurrence of plastic deformation below the eroded surface in N steel, DP3.5 steel and FMS as depicted in Figs. 5.9, 5.10, and 5.11. The extent of deformation depends on the energy absorbing capability of the steel, which in turn, is governed by the microstructure [40,95,109]. One may observe that the depth of deformation is largest for N steel and lowest for FMS due to their toughness values. It should be noted that the depth of deformation for DP3.5 steel lies in-between. The highest erosion rate shown by FMS for relatively higher velocities of 90 m/s and 120 m/s at normal angle of impact may be attributed to its brittle nature which renders it poor capability to deform and hence, a lowest depth of plastic deformation which is reflected by moderate hardness gradient, see Fig. 5.12 (b).

As far as the interference effects are concerned, the calculated probability of collision between incoming and rebounding particles by using the model proposed by Anand et al. [110]. The calculation of total probability particle collision at normal incidence is given in Eq. (5.1),

$$\mathbf{P_{tot} = 1 - exp\ (-\sigma\ Q_o\ t_r)} \qquad \text{Eq. 5.1}$$

Where P_{tot} is the total probability of first-order collision between the incident and a rebound particle, σ is the single-particle collision cross-section, Q_o is the incident particle number flux (particles cm^{-2} s^{-1}), and t_r is the average flight time of the rebounding particle.

For alumina particles with average uniform diameter D (45μm), the collision cross-section has been calculated using $\sigma = \pi D^2$ and it is found to be 1.59×10^{-5} cm^2.

Average flight time t_r has been calculated from Eq. (5.2)

$$\boldsymbol{\tau = \frac{t_r V_o}{d} = \frac{L}{d}\frac{1}{\alpha}} \qquad \text{Eq. 5.2}$$

Where τ is a dimensionless parameter to describe t_r, V_o is impact velocity, L is the average length of the flight path for rebounding particles, α is the coefficient of restitution which is taken as 0.2 (for alumina-steel pair) [110], and d is the width of the flux beam which is assumed constant.

Assuming, L= d/2, Eq. (5.3) gives,

$$\boldsymbol{\tau = \frac{1}{2\alpha}} \qquad \text{Eq. 5.3}$$

$$\mathbf{t_r} = \frac{\boldsymbol{d}}{\mathbf{2}\boldsymbol{V_o}\boldsymbol{\alpha}} \qquad \text{Eq. 5.4}$$

t_r has been calculated using Eq. (5.4) and its value for each impact velocity are listed in Table 5.3.

The value of Q_o has been calculated based on the work of [111], wherein they considered that 100 g aluminium oxide has 2×10^9 particles of 25.4 μm size. We have calculated the number of particles for a size of 45 μm (used in our study) and 100 g aluminium oxide has been found to contain 1.128 $\times10^9$ particles. Hence, the incident particle number flux for 5.4 g/min mass flow rate is found to be 5.75 $\times10^7$ particles cm^{-2} s^{-1}.

Table 5.2 shows the probability P_{tot} calculated for different velocities used under the current study, which clearly shows that P_{tot} is ~ 11% at the lowest velocity of impact used in the present study, which is quite low and decreases with increasing velocity of impact to the lowest value of ~ 3%. Hence, we believe that the 5.4 g/min erodent mass flow rate is sufficiently low to cause collisions between incoming and rebounding particles.

Table 5.2 Estimated values of P_{tot} at different impact velocities for normal impact angle

Impact velocity (V_o), m/s	30	60	90	120
Rebounding particle fight time ($t_r \times 10^{-5}$), sec.	12.5	6.25	4.167	3.125
Total probability of incident particle collision (P_{tot}), %	10.8	5.55	3.74	2.82

The subsurface cracks and micro cracks originating at or below the eroded surface see Figs. 5.8 (f) and 5.11 (c) get an easier path to propagate as they do not have to spend

energy in deformation and results in a relatively higher removal of material as seen in Figs. 5.4 ((c) and (d)). The higher plastic deformation below the surface seen for N steel may be explained on the basis of its microstructure (ferrite + pearlite) which enables it to absorb most of the particles impact energy in the form of increased depth of plastic deformation as shown in Fig. 5.11 (a) and also reflected by a relatively steeper hardness gradient, see Fig. 5.12 (b). Despite having the highest toughness, N steel has shown a higher erosion rate than DP3.5 steel, which indicates that material removal is not solely dependent on the energy absorbing capability but that other phenomena occurring at the surface (micro cutting, ridge formation, etc.) also play an important role. A relatively large amount of micro cutting and ridge formation, as shown in Fig. 5.8 (a) on the eroded surface of N steel, in addition to fractured cementite plates underneath the eroded surface, see Fig. 5.10 (a), may have provided easy access for crack propagation, resulting in a higher erosion rate compared to DP3.5 steel, as shown in Figs. 5.4 ((c) and (d)). The lowest erosion rate observed in DP3.5 steel may be attributed to an excellent combination of hardness and toughness because of its unique microstructure, which comprises of a soft and a hard phase. Hence, the depth of its plastic deformation and work hardening zone lie in-between those observed for N steel and FMS, which can be judged by a comparison of Figs. 5.9 and 5.10. A lower erosion rate in DP3.5 steel in comparison to N steel, see Figs. 5.4 ((c) and d)) despite having a low deformation zone, may again be attributed to its microstructure, wherein the cracks get arrested by the hard martensite island and inhibit their propagation, leading to only low angle cutting and micro ploughing at or below the eroded surface, see Figs. 5.8 (d) and 5.11 (b) and resulting in a relatively lower loss of removal of material [112].

The strain rates for a particle impact on a N steel, DP steels and FMS at different velocities have been calculated using Eq. (5.5) given by Hutchings [113] and the same are listed in Table 5.3.

$$\dot{\varepsilon} = \frac{2^{1.5}\, U^{0.5}}{5\pi r} \frac{(3H)^{0.25}}{(2\rho)^{0.25}} \qquad \text{Eq. 5.5}$$

Where, $\dot{\varepsilon}$ is the mean strain rate [s^{-1}], ρ *is* the erodent particle density [kg m^{-3}], r is the erodent radius [m], H is the initial hardness of the target material [kg m^{-1} s^{-2}] and U is the particle velocity [m s^{-1}]. The strain rates are found to be of the order of 10^6 s^{-1}.

Table 5.3 Estimated values of $\dot{\varepsilon}$ (strain rate) at different impact velocities for N, DP2, DP3, DP3.5, DP4 and FMS steels

Impact Velocity, m/s	**Strain rate ($\dot{\varepsilon} \times 10^6$), s^{-1}**					
	N	**DP2**	**DP3**	**DP3.5**	**DP4**	**FMS**
30	2.36	2.53	2.60	2.75	2.80	3.08
60	3.34	3.58	3.70	3.90	3.97	4.35
90	4.08	4.40	4.53	4.77	4.86	5.33
120	4.72	5.07	5.23	5.50	5.62	6.16

The strain rate for hardness test has been calculated as the ratio of the indenter velocity to the depth of indentation as suggested by [114] and the calculated values are found to be of the order of 10^{-1} s^{-1} which is significantly low in comparison to the strain rates for erosion testing.

The decrease in steady state erosion rate in the N steel, DP steels and FMS with an increase in the angle of impingement is shown in Figs. 5.4 ((a) - (d)) may be explained by considering erosion wear caused by the 15° and 90° angles of impact, except for 90° at 90 m/s and 120 m/s. At a 15° impact angle, more surface area of the target material

interacts with the erodent particles. It should be noted that at 15°, both normal as well as the shear stress component generated during impingement contribute to the formation of raised lips and subsequent removal of material in the form of chips by repeated impacts, predominantly by cutting and ploughing as evidenced by the presence of relatively deeper micro cutting marks and plastic deformation in Figs. 5.5 and 5.7 [55]. The incident of particles at relatively higher impact angles results in the formation of ridges, which get removed with the repeated impact of particles via low angle cutting. Similar observations have previously been reported [91,95].

The particles have relatively high kinetic energy and a large enough contact area with the target material to produce a significant erosion rate under a high impact velocity of 120 m/s and a low impact angle of 15°. Fig. 5.13 shows the schematic diagram of the proposed mechanism of material removal in N steel, DP3.5 steel and FMS at the 15° impact angle and 120 m/s impact velocity. In normalized steel, deep micro cutting occurs due to the impact of particles in the soft ferritic regime, as seen in SEM micrographs illustrated in Figs. 5.7 (a) and 5.9 (a). On the other hand, stacks of the pearlitic plates were deformed and resist deformation when erodent particles strike pearlitic microstructure. The shallow micro cutting and the accumulation of material take place at the beginning of the deformation of pearlite plates, which get detached by the successive impacts of particles. However, the formation of shallow craters occurs as the particles impact the relatively hard pearlitic regime; see Fig. 5.13 (a). Further, the material removal might have also occurred with the fracture and deformation of the brittle cementite lamellae. When particles are impacted on the ferritic regime, it seems to

be teared, leaving the plates exposed, resulting in a higher wear rate in the normalized steel, as illustrated in Figs. 5.7 (a) and 5.9 (a). Similar observations have also been reported earlier by Alam et al. [109]. Deep micro ploughing observed in DP3.5 steel may be attributed to the fact that the adjacent hard martensite phase might not have allowed cutting but may have only enabled material to pile up around the particle. However, when the particle hits the martensitic region, the adjacent ferrite phase does not permit it to generate micro cracks because it absorbs the majority of the impact energy due to its sufficient toughness, as depicted in Fig. 5.13 (b). A combination of hardness at an adequate level of strength endows DP3.5 steel with ample toughness, which is sufficient to absorb the energy of impacting particles and restrict cutting/surface crack formation, resulting in mild erosion. Tyagi et al. [112] have also found that dual phase structures outperform ferrite + pearlite structures in terms of wear resistance. The eroded marks of shallow craters, low angle cutting and ridge formation on the SEM micrographs, are displayed in Figs. 5.7 (d) and 5.9 (b) of DP3.5 steel supports the proposed mechanism illustrated in Fig. 5.13 (b). The proposed mechanism of material removal for FMS is given in Fig. 5.13 (c). shows only shallow micro ploughing marks as hard martensite needles do not allow deep penetration or material cutting, which is evident from SEM micrographs shown in Figs. 5.7 (f) and 5.9 (c) corresponding to FMS.

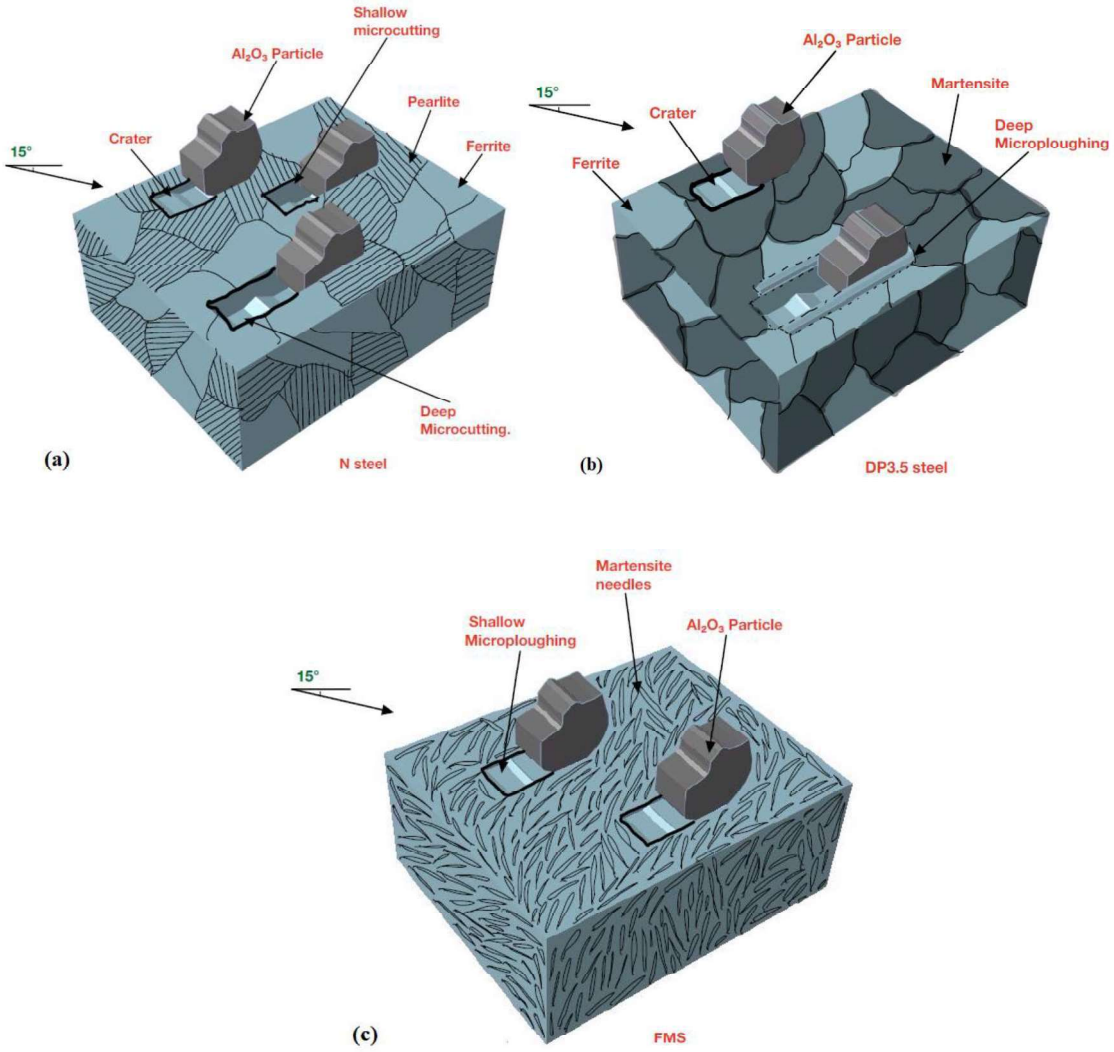

Figure 5.13 Schematic showing the proposed mechanism of material removal for (a) N steel, (b) DP3.5 steel, and (c) FMS at 15° and 120 m/s impact velocity

Figure. 5.14 shows schematic diagrams of the proposed mechanism for removing material at high impact velocities and angles, i.e., 120 m/s and 90°. The material removal in N steel illustrated in Fig. 5.14 (a) occurs by the formation of shallow craters due to the impact of a particle in the fully pearlitic region whereas ridge formation and low angle cutting take place in the ferritic region. The embedment of erodent particles also occurs if the impact is in ferritic phase. The SEM micrographs given in Figs. 5.8 (a)

and 5.11 (a) also reflect low angle cutting, ridge formation and particle embedment. When erodent particles impact the ferritic regime, the surface undergoes severe plastic deformation. Initially, the material absorbs the impact energy, but subsequent impacts cause hardening, leading to the formation of a hardened layer which gets detached, resulting in the removal of the material. The same features have been shown in the schematic of DP3.5 steel given in Fig. 5.14 (b), but the impact is mild as compared to N steel, due to the unique microstructure of DP steel, which despite being harder than N steel has an adequate amount of toughness which is comparable to N steel, as displayed in Figure. 5. SEM micrographs are shown in Figs. 5.8 (d) and 5.11 (b) for DP3.5 steel also support the formation of the same.

The schematic of FMS shown in Fig. 5.14 (c) depicts craters on the surface from which micro cracks nucleate and grow to form wide and deep craters. The surface cracking in FMS occurs at a 90° impact angle as a result of the alternating normal component of the force acting on the surface, which leads the material to experience alternate compressive and tensile plastic strains [55,109,115,116]. Initially, the micro cracks form and propagate thereafter and get connected to each other. The coalescence of cracks results in deep and wide craters, and eventually the material spalls off the target surface as shown in the proposed schematic, see Fig. 5.14 (c). The formation of micro cracks and craters could be seen in SEM micrographs, as shown in Figs. 5.8 (f) and 5.11 (c). As previously explained by other researchers, the presence of micro cracks enables the deformed surface material to be susceptible to fracture from the surface due to crack propagation between the craters [49,115,117–119]. The subsurface cracking in FMS is

expected to occur at a normal impact angle and the same has been observed in Fig. 5.11 (c). The development of voids following repeated deformation of the eroded surface layer is a prerequisite for the beginning of subsurface micro cracks. The subsurface damage may not immediately result in wear particles during erosion; it somewhat weakens the top layer, allowing the material to be removed by the impacting particles' cutting action.

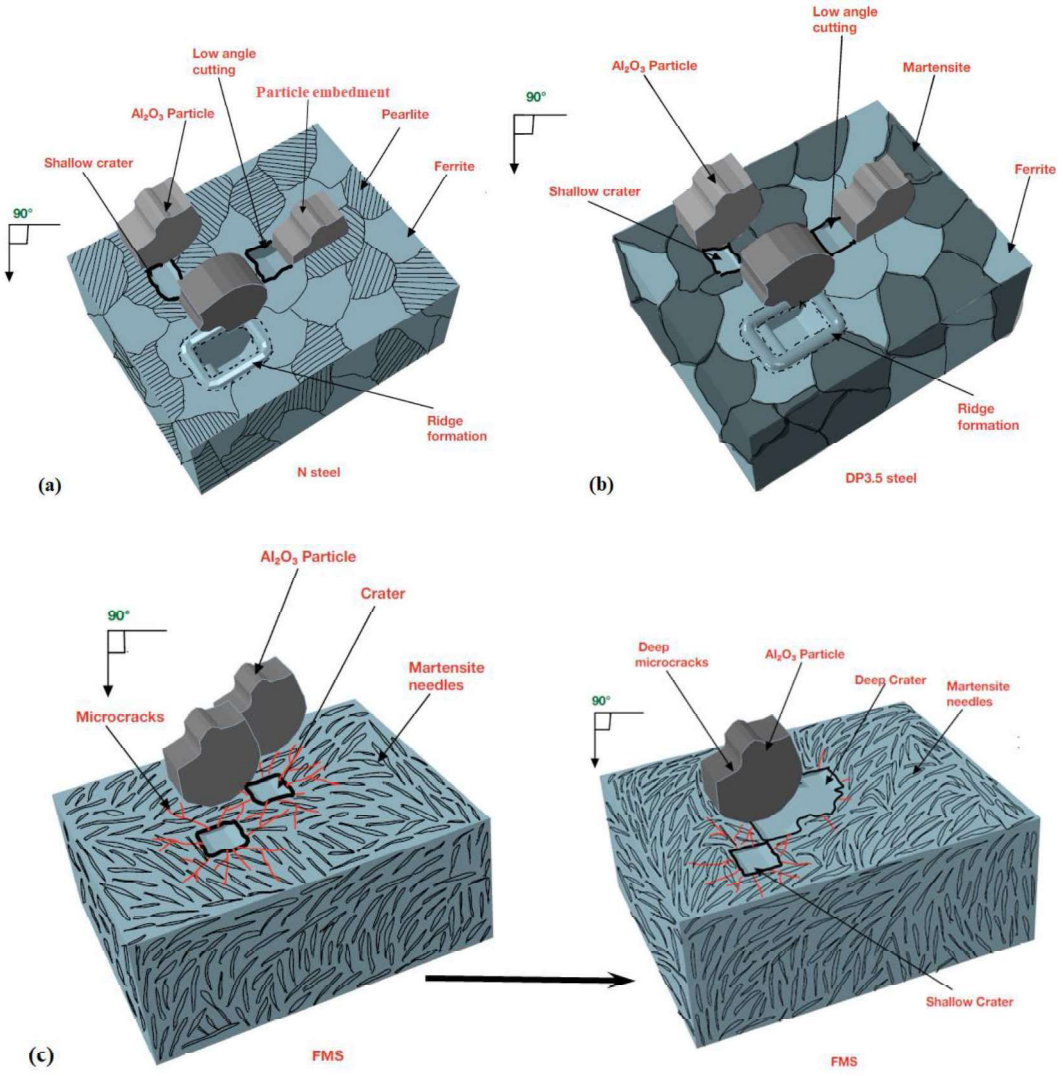

Figure 5.14 Schematic showing the proposed mechanism of material removal for (a) N steel, (b) DP3.5 steel, and (c) FMS at 90° and 120 m/s impact velocity

To summarize, the study of erosive wear presented above indicates the importance of microstructure in affecting the erosive wear of medium carbon (N), dual phase (DP), and fully martensitic (FMS) steels under various conditions. The steady state erosion rate increases with an increase in impact velocity for all materials, whereas it decreases with an increase in impact angle for all steels except for FMS. At low and high impact angles, N steel exhibits the highest erosive wear characterized by micro cutting and ridge formation. FMS has shown the highest erosion rate compared to all the steels due to its inherent brittle nature except at 90° and 120 m/s, which makes it prone to easy crack propagation. In DP steel, the cracks get arrested by the hard martensite island and their easy propagation is inhibited, which leads to only low angle cutting and micro ploughing. This reflects the advantage of using a dual phase structure. DP steels show a higher erosion resistance because they offer a balanced combination of strength and ductility at an adequate level of toughness. The material removal in N steel is found to occur by micro cutting, ridge, and crater formation, whereas shallow micro ploughing and craters are observed in FMS. However, the material removal for DP steels has been found to occur due to a combination of micro ploughing, micro cutting and crater formation.